Applied Physics Letters

Experimental evidence of absolute bandgaps in phononic crystal pipes

Cite as: Appl. Phys. Lett. **116**, 201902 (2020); https://doi.org/10.1063/5.0007532
Submitted: 13 March 2020 . Accepted: 11 May 2020 . Published Online: 19 May 2020

Jules Plisson, Adrien Pelat, François Gautier, Vicente Romero Garcia, and Thierry Bourdon

Applied Physics Letters ARTICLE scitation.org/journal/apl

Experimental evidence of absolute bandgaps in phononic crystal pipes

Cite as: Appl. Phys. Lett. **116**, 201902 (2020); doi: 10.1063/5.0007532
Submitted: 13 March 2020 · Accepted: 11 May 2020 ·
Published Online: 19 May 2020

Jules Plisson,[1,a)] Adrien Pelat,[1] François Gautier,[1] Vicente Romero Garcia,[1] and Thierry Bourdon[2]

AFFILIATIONS

[1]Laboratoire d'Acoustique de l'Université du Mans, CNRS, Av. O. Messaien, 72085 Le Mans, France
[2]Vitesco Technologies France SAS, 44 Av. du General de Croutte, 31036 Toulouse, France

[a)]**Present address:** Vitesco Technologies France SAS. **Author to whom correspondence should be addressed:** jules.plisson.etu@univ-lemans.fr

ABSTRACT

The vibration filtering properties of a phononic crystal pipe whose unit cell consists of two segments of different materials and cross sections are studied numerically and experimentally. Such an architected bi-material pipe leads to the alignment of the dispersion branches in the same frequency ranges for all types of waves (flexural, longitudinal, and torsional), leading to an absolute bandgap. Each motion is studied by a 1D model in which the propagation of Floquet–Bloch waves in lossy media is considered. Numerical optimization is based on the simplex algorithm and aims to control both the central frequency and the bandwidth of the absolute bandgap on a selected target. Experimental characterization of a demonstrator confirms the filtering effects due to partial and absolute bandgaps even in the presence of quite high structural damping.

The mitigation of noise pollution is a major societal challenge for which extensive research has been conducted[1] and NVH (Noise, Vibration, and Harshness) departments have been widely integrated notably in the transportation industry. Structure-borne sound results from bending vibrations and their couplings with other types of waves, due to the complex geometries classically encountered in industrial systems.[2] An effective reduction in the radiated sound levels then requires us to mitigate all types of waves. In this context, the approach presented here concerns the design of "total filters" that can be inserted into engine components acting as structural waveguides that transmit vibrations to other components able to radiate sound. To reach such total filter features, the design strategy is based on the concept of absolute bandgap.

The control of elastic waves by periodic structures has been dramatically developed during the last few decades by using Phononic Crystals (PCs)[3,4] as analogously done for light waves by Photonic crystals.[5] These systems, made of either periodic distributions of scatterers embedded in a physically dissimilar host material or simply periodic geometries, are driven by a particular dispersion relation showing bandgaps,[6,7] ranges of frequencies produced by the Bragg interference in which the propagation of waves is forbidden.[8] Significant progress has been made on the control of flexural or longitudinal waves by PCs showing different applications including filtering,[9,10] wave trapping,[11,12] wave-guiding,[13] focusing by refracting[14,15] or scattering[16] waves, and self-collimation,[17,18] among others.[4] One of the main challenges of PCs has been the design of absolute bandgaps over which the propagation of all elastic waves is forbidden, whatever their polarization and wave vector.

PCs with a fluid-type host medium, known as sonic crystals,[9] have theoretically and experimentally reported absolute bandgaps in broad ranges of frequencies.[10,19,20] These systems represent the most simple PC as only longitudinal waves are propagating in the medium. Perhaps the most known application of sonic crystals is the design of tunable sound screens.[21–23] However, once the host medium is a solid, the problem becomes more complex as different polarisation can be excited in the system. In this case, theoretical evidence of absolute bandgaps is also widely reported in the literature. 1D PCs exhibiting absolute bandgaps have been analyzed by the transfer matrix method,[24] and recently, 1D PCs with alternating materials in the radial and axial directions have been used to show absolute bandgaps.[25] Two-dimensional (2D) PC slabs consisting of either solid[26] or piezoelectric[27] inclusions placed periodically in an isotropic host material have been theoretically analyzed, showing absolute bandgaps with a variable bandwidth for elastic waves of any polarization and incidence. Bulk 2D PCs have also been proposed for bulk wave attenuation with solid[28] or magnetostrictive[29] inclusions. Using specialized

genetic algorithms, 2D PCs formed from silicon and solid voids have been optimized to obtain unit cell designs exhibiting absolute bandgaps for both in- and out-of-plane motions.[30]

From the experimental point of view, absolute bandgaps have also been reported in the literature. 2D binary solid/solid composite media with cylindrical inclusions embedded in an epoxy resin matrix showed dips of transmission, evidencing the presence of absolute bandgaps.[31] More recently, the presence of absolute bandgaps in pillared PC slabs has been shown by double-vibrator three-components[32] and temperature-driven adaptive systems.[33] 3D PCs made of face-centered cubic unit cells composed of a single material have been used to experimentally show ultra-wide absolute bandgaps.[34,35] Recently, 3D load-bearing architected lattices, composed of a single material, have been designed for presenting broadband frequency bandgaps for all directions and polarizations for airborne sound and elastic vibrations simultaneously.[36] However, although 2D and 3D PCs have been widely validated experimentally, less attention has been paid to the experimental analysis of 1D cases acting simultaneously on longitudinal, flexural, and torsional waves. The control of vibrations in such 1D PC systems can impact the design of piping systems, which can be exploited in areas such as the automotive industry, heat exchanger tubes in chemical plants, oil pipelines, marine risers, and pump discharge lines, among others.[37]

In this work, we apply the concept of absolute bandgap in order to design and experimentally validate 1D PC pipes able to mitigate longitudinal, flexural, and torsional waves in the same target band. A 1D PC pipe made of a unit cell consisting of two different hollow cylinders made of aluminum and nylon (see Fig. 1) is optimized. Considering lossy constitutive materials, the eigenvalue problems of the three types of waves are analytically solved by imposing continuity conditions between the different parts of the unit cell and Floquet–Bloch periodic conditions at its extremities. The three problems are combined via a minimizing algorithm in order to reach the geometry of the 1D PC pipe that exhibits an absolute bandgap of target central frequency and bandwidth. Full 3D finite element simulations and experimental characterization of a demonstrator of finite size are in good agreement and show dips in the transfer functions associated with the predicted absolute bandgap.

Figures 1(a)–1(d) show the images of the 1D bi-material PC pipe used in the experiments. A detailed scheme with the geometrical parameters of the system is shown in Figs. 1(e) and 1(f). Each segment of the unit cell is assumed to be a thin-walled pipe of annular cross section. We define $\gamma = l_2/l_{tot}$ as the length ratio and $\beta = R_2/R_1$ as the outer radius ratio. The inner radius R_{int} is constant for the two segments of the unit cell. These two geometrical parameters will be used to describe the geometry in the optimization procedure. The 1D PC pipe is made of aluminum and nylon, considered as linear and isotropic elastic materials. Nylon is characterized by its Young modulus $E_N = 2.3$ GPa, its density $\rho_N = 1240$ kg/m^3, and its Poisson ratio $\nu_N = 0.3$. The aluminum characteristics are $E_A = 71$ GPa, $\rho_A = 2170$ kg/m^3, and $\nu_A = 0.3$.

Here, we consider harmonic wave motion with the time convention $e^{i\omega t}$. In what follows, the subindex $i = N, A$ and the superindex $w = l, t$ will represent each segment of the unit cell and the wave type (longitudinal, l, or torsional, t), respectively. On the one hand, the propagation of longitudinal and torsional waves in the i-th part of the unit cell is modeled by a 1D Helmholtz equation,[38]

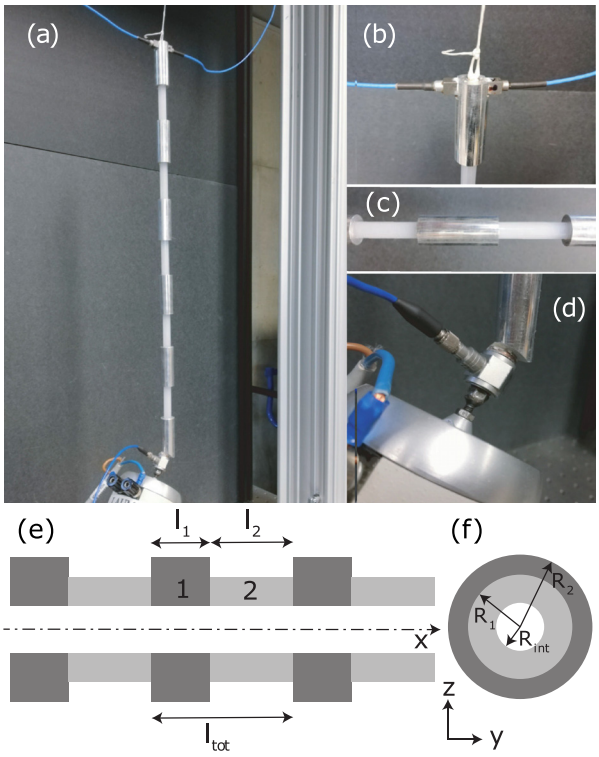

FIG. 1. Scheme and images of the manufactured PC pipe. Nylon and aluminum sections are nested by force fitting, which holds the assembly together without the use of glue and, therefore, minimizes unwanted losses. (a) Experimental setup; (b) details of the 2 face-to-face three-axis accelerometers; (c) view of the 2 aluminum/nylon unit cells of the demonstrator; (d) view of the shaker excitation implemented at the oblique position such that all wave types are excited. (e) and (f) show lateral and cross-sectional schematic representation of the modeled PC pipe, respectively.

$$\frac{\partial^2 u_i^w}{\partial x^2} + (k_i^w)^2 u_i^w = 0, \tag{1}$$

where u_i^w is the displacement of wave w of the i-th segment of the unit cell. $k_i^w = \frac{\omega}{c_i^w}$ is the wave number, with $c_i^w = \sqrt{E_i^w/\rho_i}$ being the speed of the wave; $E_i^l = E_i$ is the Young modulus, and $E_i^t \equiv G_i = E_i/2(1+\nu_i)$ is the shear modulus.

On the other hand, flexural waves are described using Timoshenko's beam theory[39,40] that takes into account shear deformation and rotational inertia effects. Even this framework is based on low frequency assumptions; this makes it possible to analyze the propagation at higher frequencies or for thicker beams than with Euler–Bernoulli's theory. Following Timoshenko assumption, the flexural displacement v_i satisfies the motion equation,

$$\frac{E_i}{\rho_i}\frac{\partial^4 v_i}{\partial x^4} + \omega^2\left(1 + \frac{E_i}{\kappa_i G_i}\right)\frac{\partial^2 v_i}{\partial x^2} + \left(\frac{S_i\omega^2}{I_i} - \frac{\rho_i I_i \omega^4}{\kappa_i G_i}\right)v_i = 0, \tag{2}$$

where κ_i, S_i, and I_i are the shear coefficient, the cross-sectional area, and quadratic moment, respectively. In order to obtain the eigenvalue problem whose solutions give the complex dispersion relation, $k_b = k(\omega)l_{tot}/\pi$, we apply the continuity boundary conditions at the interfaces between each segment of the unit cell as well as the

Floquet–Bloch periodic conditions at its extremities (see the supplementary material for more details). The resulting set of equations leads to a linear system $M(\omega, k_b).\mathbf{B} = \mathbf{0}$, where for each given ω of a frequency range of interest, the values of k_b satisfying $\det(M) = 0$ are found numerically to provide the dispersion relation. By solving each 1D model in this way, we obtain the dispersion relations for all types of waves in the PC pipe. Solutions obtained by the previous semi-analytical methodology are compared with reference solutions provided by 3D elasticity finite element simulations (solid mechanics COMSOL package).

Figure 2(a) shows the real part of the dispersion relation for a PC pipe with the following geometry: $l_{tot} = 0.1$ m, $\gamma = 0.2$, $R_1 = 8$ mm, and $\beta = 0.5$. Colored dots (each color a wave type) represent the results obtained from the semi-analytical model, while gray circles represent the FEM reference solutions. The results are in very good agreement, and so the semi-analytical modeling is well validated. However, some disagreements appear for flexural waves at high frequencies (dispersion branch just under 20 kHz) due to the expected limitations of Timoshenko's beam model. Anyway, the dispersion relation obtained for this geometrical layout exhibits a wide absolute bandgap in the range of [3–10] kHz.

Figure 2(b) shows the evolution of the bandgaps as β changes. Each colored patch in the plot encloses the frequencies between the lower and the upper edge of the bandgap. The results indicate that β essentially controls the bandgap bandwidth and has a relatively weak effect on their central frequencies. Such tendency has already been observed in the case of monolithic corrugated beams.[41]

Analogously, Fig. 2(b) shows the evolution of the bandgaps as γ changes. Both the central frequency and the width display

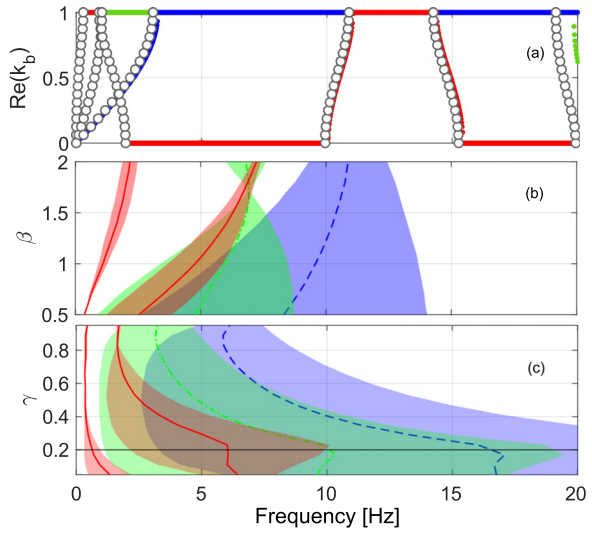

FIG. 2. Analysis of the dispersion relation of a bi-material PC pipe with $l_{tot} = 0.1$ m; (a) Real part of the dispersion relation with $\gamma = 0.2$, $R_1 = 8$ mm, and $\beta = 0.5$ calculated by both the semi-analytical model (colored dots, (blue) longitudinal, (red) flexural, and (green) torsional) and 3D full FEM simulation (open circles °); (b) and (c) evolution of the bandgap widths (colored patches) and mid frequencies (lines) for the three wave types [the same color legend as in (a)] as a function of (b) β with $\gamma = 0.5$ and (c) γ with $\beta = 0.5$. $l_{tot} = 0.1$ m. The horizontal black line denotes the configuration leading to the dispersion graph in (a).

nonmonotonous variations of the same range. In particular, some optimal band widths appear around $\gamma = 0.2$. Finally, γ has a more complex effect on the bandgap features that do not follow any clearly identifiable law. Anyway, there are some configurations for which all bandgaps overlap, creating an absolute bandgap. This feature is obtained in the range of $[4 - 10]$ kHz for $\gamma = 0.2$, for example. In this case, the second flexural bandgap and the first longitudinal and torsional bandgaps are involved. However, Figs. 2(b) and 2(c) show that it is difficult to tune by hand the absolute bandgap to a target band. In order to achieve this goal, a numerical optimization procedure is proposed below.

A Nelder–Mead local minimisation algorithm[42] is used in this work to provide the geometrical parameters of a PC pipe with an absolute bandgap defined from both a target central frequency f_0 and a target bandwidth Δf_0. The set of parameters subject to the optimization is defined as $X = [l_{tot}, \gamma, R_1, \beta]$. It is worth noting here that the first unit cell segment will be made of aluminum and the second one of nylon. The cost function $\mathscr{F}$ is defined as a weighted sum of two convergence indicators and reads

$$\mathscr{F} = \alpha_{f_c} I_{fc} + \alpha_{\Delta f} I_{\Delta f}. \tag{3}$$

The weighting coefficients α_{f_c} and $\alpha_{\Delta f}$ are adjustable such that $\alpha_{f_c} + \alpha_{\Delta f} = 1$, and the convergence indicators are defined by

$$I_{\Delta f} = \left| 1 - \frac{\Delta f - \Delta f_0}{\Delta f + \Delta f_0} \right|, \tag{4}$$

$$I_{fc} = \left| 1 - \frac{f_c - f_0}{f_c + f_0} \right|, \tag{5}$$

with $\Delta f = \min\left(f_{max}^{(i)}\right) - \max\left(f_{min}^{(i)}\right)$ being the absolute bandwidth and $f_c = \frac{1}{2}\left[\max\left(f_{min}^{(i)}\right) + \min\left(f_{max}^{(i)}\right)\right]$ the central frequency. $f_{max,min}^{(i)}$ represents the upper (index *max*) and lower (index *min*) edges of the bandgap for the i-th wave, where the subindex i represents each type of wave type $i = F, L, T$ for flexural, longitudinal, and torsional waves, respectively. I_{f_c} and $I_{\Delta f}$ evaluate the deviation between the bandgap features f_c and Δf and the target features f_0 and Δf_0, respectively. These definitions are chosen so that the cost function is unitary $(0 < \mathscr{F} < 1)$.

This optimization procedure is applied to the solution of the semi-analytical eigenvalue problems described above with a target absolute bandgap of [3–6] kHz, which is a typical range of interest for injection applications in the context of automotive industry.[43] A detailed study of the optimization is given in the supplementary material and concludes that to ensure both accuracy and fast convergence, the best choice for the weighting coefficient of the cost function is $[\alpha_{f_c}, \alpha_{\Delta f}] = [5/6, 1/6]$. The optimal geometry of the 1D PC pipe obtained under these conditions and without considering material losses is $X = [87\text{ mm}, 0.44, 7.5\text{ mm}, 0.5]$. From the optimized geometry in the conservative case, the final complex dispersion relation of the PC pipe shown in Fig. 3(a) is calculated considering the viscoelastic losses for both aluminum and nylon via the complex Young modulus $E_i^c = E_i(1 + \imath\eta_i)$, with $\eta_A = 1 \times 10^{-4}$ and $\eta_N = 4 \times 10^{-2}$. Each wave type displays bandgaps where the real part of the wavenumber is low, while imaginary part is high [see the colored patches in Fig. 3(b)]. In the target range of frequencies, bandgaps are well overlapping, and the obtained absolute bandgap is [3.2–5.7] kHz [gray patch in Fig. 3(a)], which is slightly narrower than the target, due to the losses.

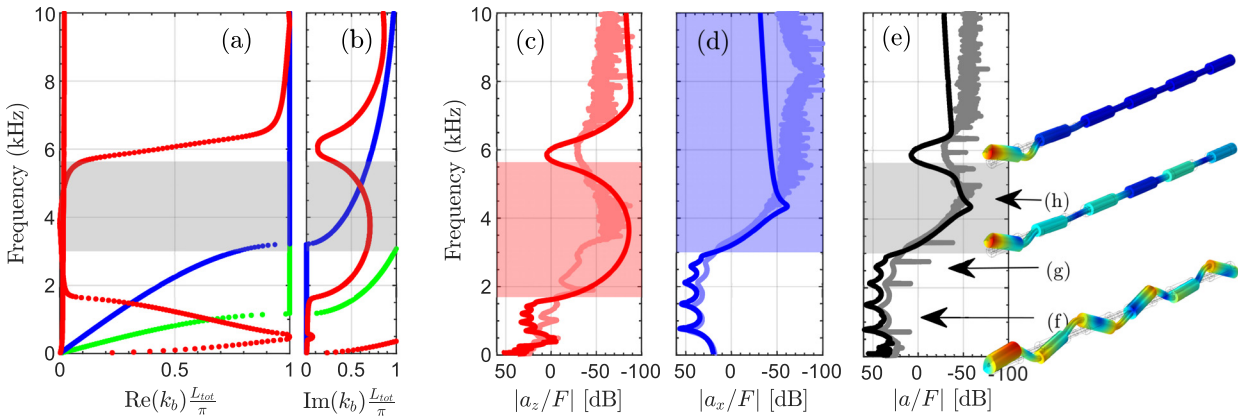

FIG. 3. Numerical analysis and experimental characterisation of the optimal PC pipe: (a) real part and (b) imaginary part of the optimized complex dispersion relation obtained by the Floquet–Bloch method and considering the viscoelastic losses (see the main text). (blue) Longitudinal, (red) flexural, and (green) torsional; measured (light line) and simulated (dark line) acceleration transfer functions in the (c) flexural, (d) longitudinal, and (e) full loading cases; 3D views of the simulated total displacement in the full loading case at (f) 900 Hz where all wave types propagate, (g) 2500 Hz where only the flexural bandgap is opened, and (h) 4500 Hz within the absolute bandgap.

In order to experimentally evaluate the vibration mitigation performances due to the absolute bandgap of the infinite PC pipe, a finite pipe demonstrator with 6 unit cells is manufactured [Fig. 1(a)]. In the experimental setup, the demonstrator is suspended vertically from rigid gallows mounted on an optical breadboard. A shaker (LDS V201) excites the demonstrator at its bottom end with a harmonic point force $\boldsymbol{F} = F_x.\boldsymbol{x} + F_y.\boldsymbol{y} + F_z.\boldsymbol{z}$ [see the axis definition in Figs. 1(e) and 1(f)] with a step-by-step sine in the range of [0–10] kHz with a frequency step of 5 Hz. 3 cases are considered: "flexural loading" such as $F_z \neq 0$ and $F_x = F_y = 0$ (when the shaker is perpendicular to the pipe x-axis, only flexural waves are excited), "longitudinal loading" such as $F_x \neq 0$ and $F_y = F_z = 0$ (when the shaker is aligned with the pipe x-axis, only longitudinal waves are excited), and "full loading" such as $F_{x,y,z} \neq 0$ as shown in Fig. 1(d) where the force of the shaker is applied obliquely on a cut plane and off-centre with respect to the pipe x-axis so that all wave types are generated. The acceleration response $\boldsymbol{a} = a_x.\boldsymbol{x} + a_y.\boldsymbol{y} + a_z.\boldsymbol{z}$ is measured at the upper end using 2 three-axial accelerometers (PCB 356A01) that face each other [Fig. 1(b)]. This experimental situation is also numerically simulated from a full wave 3D FEM model in order to compare transfer functions.

Figure 3(c) represents both numerical and experimental transfer functions $|a_z/F|$ in the flexural loading case. The transfer functions show an attenuation of about 70 dB in the frequency range corresponding to the predicted flexural bandgap. The same trend is exhibited in Fig. 3(d) that plots the transfer functions $|a_x/F|$ in the longitudinal loading case. Finally, the full loading case is shown in Fig. 3(e), evidencing a strong attenuation in the transfer function $|a/F|$ in the range corresponding to the predicted absolute bandgap. It is also worth noting that finite size effects can be seen at low frequencies with peaks of the transfer function corresponding to the Fabry–Pérot resonances of the system.

To complete the analysis, 3D views of the simulated total displacement field in the full loading case are shown in Figs. 3(f)–3(h). At 900 Hz where all wave types propagate [Fig. 3(f)], the superposition of all motions results in a complex total displacement field. At 2.5 kHz [Fig. 3(g)], the field mainly exhibits the longitudinal component, with the flexural component being strongly attenuated due to the bandgap effect. At 4.5 kHz [Fig. 3(h)], the total field vanishes close to the excitation due to the total filtering effect associated with the absolute bandgap.

To summarize, we apply the concept of absolute bandgap to a bi-material PC pipe. Three 1D analytical Floquet–Bloch models giving the dispersion of longitudinal, flexural, and torsional waves considering losses are combined in an optimization procedure to reach a unit cell design that exhibit absolute bandgaps with target features. The hand ability and reliability of such design methodology are shown through a set of cases detailed in the supplementary material, which brings a first main insight. On the top of that, the study of a 6-cell demonstrator shows both numerically and experimentally dips of the transfer functions corresponding to the absolute bandgap analytically predicted, bringing a second main insight. These results illustrate how absolute bandgaps in the high frequency domain can be applied to mitigate vibrations that may result in structure-borne sound in some industrial systems. In further works, the design and optimization of such PC pipes would be extended considering an enclosed pressurized liquid, hence considering couplings between acoustic and elastic waves.

See the supplementary material for both the analytical wave dispersion models and the numerical optimization procedure and its application to a set of optimization cases.

The authors thank the Vitesco Technologies company and ANRT French agency who funded this research, Julien Nicolas and Stanislas Renard who manufactured the demonstrator, and Félix Foucard for his fruitful contribution in the experiments.

DATA AVAILABILITY

The data that support the findings of this study are available from the corresponding author upon reasonable request.

REFERENCES

[1]M. Crocker, *Handbook of Noise and Vibration Control*, 3rd ed. (John Wiley & Sons, New Jersey, 2007).

[2]L. Cremer, M. Heckl, and B. A. T. Petersson, *Structure-Borne Sound: Structural Vibrations and Sound Radiation at Audio Frequencies*, 3rd ed. (Springer, Berlin; New York, 2005).
[3]*Acoustic Metamaterials and Phononic Crystals*, edited by P. Deymier (Springer, 2013).
[4]*Fundamentals and Applications of Acoustic Metamaterials: From Seismic to Radio Frequency*, edited by V. Romero-García and A.-C. Hladky-Hennion (Wiley-ISTE, 2019).
[5]J. D. Joannopoulus, S. G. Johnson, J. N. Winn, and R. D. Meade, *Photonic Crystals. Molding the Flow of Light* (Princeton University Press, 2008).
[6]E. Economou and M. Sigalas, "Classical wave propagation in periodic structures: Cermet versus network topology," Phys. Rev. B **48**(18), 13434 (1993).
[7]M. Kushwaha, P. Halevi, L. Dobrzynski, and B. Djafari-Rouhani, "Acoustic band structure of periodic elastic composites," Phys. Rev. Lett. **71**, 2022–2025 (1993).
[8]L. Brillouin and M. Parodi, *Propagation Des Ondes Dans Les Milieux Périodiques* (Masson et Cie, 1956).
[9]R. Martínez-Sala, J. Sancho, J. V. Sánchez, V. Gómez, J. Llinares, and F. Meseguer, "Sound attenuation by sculpture," Nature **378**, 241 (1995).
[10]J. V. Sánchez-Pérez, D. Caballero, R. Martínez-Sala, C. Rubio, J. Sánchez-Dehesa, F. Meseguer, J. Llinares, and F. Gálvez, "Sound attenuation by a two-dimensional array of rigid cylinders," Phys. Rev. Lett. **80**, 5325–5328 (1998).
[11]M. Sigalas and E. Economou, "Elastic and acoustic wave band structure," J. Sound Vib. **158**, 377 (1992).
[12]A. Khelif, A. Choujaa, B. Djafari-Rouhani, M. Wilm, S. Ballandras, and V. Laude, "Trapping and guiding of acoustic waves by defect modes in a full-band-gap ultrasonic crystal," Phys. Rev. B **68**, 214301 (2003).
[13]A. Khelif, M. Wilm, V. Laude, S. Ballandras, and B. Djafari-Rouhani, "Guided elastic waves along a rod defect of a two-dimensional phononic crystal," Phys. Rev. E **69**, 067601 (2004).
[14]F. Cervera, L. Sanchis, J. V. Sánchez-Pérez, R. Martínez-Sala, C. Rubio, and F. Meseguer, "Refractive acoustic devices for airborne sound," Phys. Rev Lett. **88**, 023902–023904 (2002).
[15]S.-C. Lin, T. Huang, J.-H. Sun, and T.-T. Wu, "Gradient-index phononic crystals," Phys. Rev. B **79**, 094302 (2009).
[16]L. Feng, X. Liu, Y. Chen, Z. Huang, Y. Mao, Y. Chen, J. Zi, and Y. Zhu, "Negative refraction of acoustic waves in two-dimensional sonic crystals," Phys. Rev. B **72**, 033108 (2005).
[17]I. Pérez-Arjona, V. J. Sánchez-Morcillo, J. Redondo, V. Espinosa, and K. Staliunas, "Theoretical prediction of the nondiffractive propagation of sonic waves through periodic acoustic media," Phys. Rev. B **75**, 014304 (2007).
[18]A. Cebrecos, V. Romero-García, R. Picó, I. Pérez-Arjona, V. Espinosa, V. J. Sánchez-Morcillo, and K. Staliunas, "Formation of collimated sound beams by three-dimensional sonic crystals," J. Appl. Phys. **111**, 104910 (2012).
[19]V. Romero-García, J. Sánchez-Pérez, S. C. neira Ibáñez, and L. Garcia-Raffi, "Evidences of evanescent bloch waves in phononic crystals," Appl. Phys. Lett. **96**, 124102 (2010).
[20]A. Cebrecos, V. Romero-García, and J. P. Groby, "Complex dispersion relation recovery from 2D periodic resonant systems of finite size," Appl. Sci. **9**, 478 (2019).
[21]J. Sánchez-Pérez, C. Rubio, R. Martínez-Sala, R. Sánchez-Grandia, and V. Gómez, "Acoustic barriers based on periodic arrays of scatterers," Appl. Phys. Lett. **81**, 5240 (2002).
[22]V. Romero-García, J. V. Sánchez-Pérez, and L. M. Garcia-Raffi, "Tunable wide-band bandstop acoustic filter based on two-dimensional multiphysical phenomena periodic systems," J. Appl. Phys. **110**, 14904 (2011).
[23]T. Cavalieri, A. Cebrecos, J.-P. Groby, C. Chaufour, and V. Romero-García, "Three-dimensional multiresonant lossy sonic crystal for broadband acoustic attenuation: Application to train noise reduction," Appl. Acoust. **146**, 1–8 (2019).
[24]H. Shen, J. Wen, D. Yu, and X. Wen, "The vibrational properties of a periodic composite pipe in 3d space," J. Sound Vib. **328**, 57–70 (2009).
[25]Y. Zhang, D. Yu, and J. Wen, "Study on the band gaps of phononic crystal pipes with alternating materials in the radial and axial directions," Extreme Mech. Lett. **12**, 2–6 (2017).
[26]J. O. Vasseur, P. A. Deymier, B. Djafari-Rouhani, Y. Pennec, and A.-C. Hladky-Hennion, "Absolute forbidden bands and waveguiding in two-dimensional phononic crystal plates," Phys. Rev.B **77**, 085415 (2008).
[27]A. Khelif, B. Aoubiza, S. Mohammadi, A. Adibi, and V. Laude, "Complete band gaps in two-dimensional phononic crystal slabs," Phys. Rev. E **74**, 046610 (2006).
[28]M. S. Kushwaha, P. Halevi, G. Martínez, L. Dobrzynski, and B. Djafari-Rouhani, "Theory of acoustic band structure of periodic elastic composites," Phys. Rev. B **49**(4), 2313–2322 (1994).
[29]J.-F. Robillard, O. B. Matar, J. O. Vasseur, P. A. Deymier, M. Stippinger, A.-C. Hladky-Hennion, Y. Pennec, and B. Djafari-Rouhani, "Tunable magnetoelastic phononic crystals," Appl. Phys. Lett. **95**, 124104 (2009).
[30]O. R. Bilal and M. I. Hussein, "Ultrawide phononic band gap for combined in-plane and out-of-plane waves," Phys. Rev. E **84**, 065701 (2011).
[31]J. O. Vasseur, P. A. Deymier, G. Frantziskonis, G. Hong, B. Djafari-Rouhani, and L. Dobrzynski, "Experimental evidence for the existence of absolute acoustic band gaps in two-dimensional periodic composite media," J. Phys.: Condens. Matter **10**, 6051–6064 (1998).
[32]H.-J. Zhao, H.-W. Guo, M.-X. Gao, R.-Q. Liu, and Z.-Q. Deng, "Vibration band gaps in double-vibrator pillared phononic crystal plate," J. Appl. Phys. **119**, 014903 (2016).
[33]K. Billon, M. Ouisse, E. Sadoulet-Reboul, M. Collet, P. Butaud, G. Chevallier, and A. Khelif, "Design and experimental validation of a temperature-driven adaptive phononic crystal slab," Smart Mater. Struct. **28**, 035007 (2019).
[34]T. Delpero, S. Schoenwald, A. Zemp, and A. Bergamini, "Structural engineering of three-dimensional phononic crystals," J. Sound Vib. **363**, 156–165 (2016).
[35]L. D'Alessandro, E. Belloni, R. Ardito, A. Corigliano, and F. Braghin, "Modeling and experimental verification of an ultra-wide bandgap in 3D phononic crystal," Appl. Phys. Lett. **109**, 221907 (2016).
[36]O. R. Bilal, D. Ballagi, and C. Daraio, "Architected lattices for simultaneous broadband attenuation of airborne sound and mechanical vibrations in all directions," Phys. Rev. Appl. **10**, 054060 (2018).
[37]G. Koo and Y. Park, "Vibration analysis of a 3-dimensional piping system conveying fluid by wave approach," Int. J. Pressure Vessels Piping **67**, 249–256 (1996).
[38]K. F. Graff, *Wave Motion in Elastic Solids* (Dover Publications, 1975).
[39]L. Liu and M. I. Hussein, "Wave motion in periodic flexural beams and characterization of the transition between Bragg scattering and local resonance," J. Appl. Mech. **79**, 011003 (2012).
[40]A. Hvatov and S. Sorokin, "Free vibrations of finite periodic structures in pass- and stop-bands of the counterpart infinite waveguides," J. Sound Vib. **347**, 200–217 (2015).
[41]A. Pelat, T. Gallot, and F. Gautier, "On the control of the first bragg band gap in periodic continuously corrugated beam for flexural vibration," J. Sound Vib. **446**, 249–262 (2019).
[42]J. C. Lagarias, J. A. Reeds, M. H. Wright, and P. E. Wright, "Convergence properties of the Nelder–Mead simplex method in low dimensions," SIAM J. Optim. **9**, 112–147 (1998).
[43]T. Bourdon, R. Weber, and J. Massinger, "Virtual nvh prototyping of fuel components design—Focus on high pressure pumps and SCR injectors," in *SAE Technical Paper* (SAE International, 2017).